

Powder bed fusion of AlSi10Mg using an electron beam - Processability, microstructure and mechanical properties

Robert Ortmann (M. Sc.)^a, Nele Kretzer (M. Sc.)^a, Dr.-Ing. Tobias Grimm^a,
Prof. Dr.-Ing. Jan T. Sehr^a

^a Ruhr-Universität Bochum, Universitätsstraße 150, 44801 Bochum, Deutschland

https://doi.org/10.58134/fh-aachen-rte_2024_001

Zusammenfassung Das pulverbettbasierte Schmelzen von Metallen mittels Elektronenstrahl (PBF-EB/M) und Laserstrahl (PBF-LB/M) sind additive Fertigungsverfahren zur endkonturnahen schichtweisen Herstellung komplexer Bauteile, die in DIN EN ISO/ASTM 52900 genormt sind. Obwohl die Fertigungsverfahren in Forschung und Industrie weit verbreitet sind, werden Aluminiumlegierungen mit hoher spezifischer Festigkeit, wie beispielsweise AlSi10Mg, nur im Bereich des PBF-LB/M verarbeitet und untersucht. Experimentelle Untersuchungen im Bereich des PBF-EB/M mit einer punktbasierten Belichtungsstrategie existieren jedoch bisher nicht. Basierend auf der Charakterisierung des Pulverwerkstoffs untersucht diese Studie die Verarbeitbarkeit, die Elementverflüchtigung und die Eigenschaften von AlSi10Mg-Proben, die durch PBF-EB/M hergestellt wurden. Die Ergebnisse werden anschließend mit den Eigenschaften verglichen, die in der wissenschaftlichen Literatur durch das PBF-LB/M-Verfahren erzielt werden. Die hergestellten Proben erreichen eine relative Dichte von 99,9 % und eine Vickershärte von bis zu 52 HV1. Die mechanischen Eigenschaften zeigen im Vergleich zum PBF-LB/M geringere Zugfestigkeiten von bis zu 152 MPa, aber eine verbesserte Bruchdehnung von bis zu 27 %.

Abstract Powder bed fusion additive manufacturing processes of metals using an electron beam (PBF-EB/M) and a laser beam (PBF-LB/M) are methods for producing complex near-net-shape parts layer upon layer, which are standardized in DIN EN ISO/ASTM 52900. Although the manufacturing processes are extensively used in research and industry, the processing of aluminum alloys with high specific strength, such as AlSi10Mg, is only applied and scientifically covered in laser powder bed fusion, but not yet in electron beam powder bed fusion using a spot-based exposure approach. Based on powder feedstock characterization, this study focuses on the processability, element evaporation, and properties of AlSi10Mg samples processed by electron beam powder bed fusion. Obtained properties are compared with those reported for AlSi10Mg processed by PBF-LB/M. Manufactured samples achieve 99.9 % relative density and a Vickers hardness of up to 52 HV1. Tensile properties show lower tensile strengths of up to 152 MPa but superior elongation at break values of up to 27 % compared to PBF-LB/M.

Introduction

Additive manufacturing offers new possibilities in component design, such as creating complex geometries without part-specific tools. Powder bed fusion processes of metals using an electron beam (PBF-EB/M) and a laser beam (PBF-LB/M) are additive manufacturing methods in which thermal energy selectively fuses regions of a powder bed to produce complex near-net-shape parts. The PBF processes are standardized in DIN EN ISO/ASTM 52900 [1]. Especially in PBF-LB/M, the processing of aluminum alloys such as AlSi10Mg is widely studied [2]. Parts are used in different industries such as automotive, manufacturing in aerospace and defense, and machinery as well as tools production [3]. However, in the field of PBF-EB/M, the processability of aluminum alloys is widely uncovered as aluminum is primarily present as an alloying element in TiAl alloys and used in medical [4] and high-temperature applications [5–7].

In addition to the studies conducted and published by the authors [8], Bian et al. [9] published a study on the heat treatment of the microstructure of AlSi10Mg using PBF-EB/M as an additive manufacturing technique. The authors achieve a density of almost 100 % and tensile ductilities between 25.9 % and 32.7 %, which exceed the elongations at break previously reported and performed in the PBF-LB/M process. However, the authors use a vector-based exposure strategy. Therefore, the point-based exposure used in this study is a novelty for processing AlSi10Mg. To facilitate a comparison with the existing literature referenced before, samples manufactured with a vector-based exposure are also included in this study.

The evaporation of alloying elements can mainly be observed in the high vacuum and high peak-temperature conditions in PBF-EB/M-processes [6]. The high processing temperatures and low ambient pressure promote the evaporation of elements with high vapor pressure. A change in the alloying constituents significantly influences the mechanical properties of the manufactured components in terms of strength values, corrosion resistance, and ductility [10]. PBF-EB/M reaches very high temperatures locally, which can exceed the boiling point of the respective material constituents, especially volatile elements. The high local temperatures complicate the production of components subject to very narrow specification limits in terms of their chemical composition [7]. A correlation of the rate of change of material volatilization as a function of volume energy density (VED) has already been demonstrated in the preliminary work of the authors using an AlSi10Mg alloy with a vector-based exposure strategy [8]. By calculating the VED [11], the local energy input into the material is quantified as a function of the beam power, the scanning speed, the hatch distance, and the layer thickness. The reduction of the aluminum content compared to the initial concentration is more distinct at a power of 300 W compared to test specimens produced at 200 W [8]. Although the VED is the same, at 300 W it is introduced into the material in a shorter time, resulting in higher processing temperatures and increased volatilization of aluminum [8]. A reduction in aluminum loss has also been reported by reducing the VED when processing a TiAl alloy, mainly influenced by line energy density, i.e., the beam power/beam speed ratio [7].

Typically, PBF-EB/M-processes use the common vector-based cross-section scanning strategies for part production, also known from PBF-LB/M. However, it has been shown that achieving high beam velocities through electromagnetic deflection enables the implementation of new scanning algorithms, such as spot-based exposure algorithms. Spot-based exposure strategies divide the cross-section into discrete points based on a

defined point spacing, for which a sequence and dwell time are specified [12]. The local energy input directly relates to the dwell time at constant point distances. Optimization of point sequence allows the control of local solidification and, thus, site-specific control of crystallographic grain structure, orientation, size, and spacing of dendrite arms [13–18]. However, Lee et al. [12] also acknowledge the return time, i.e., the time between the melting of two adjacent points must be considered in addition to exposure power, point distance, and dwell time to achieve consistent results and microstructures.

Materials and Methods

This study used gas-atomized AlSi10Mg powder acquired from the company IMR and sampled according to the standard DIN EN ISO 3954 [19] for powder characterization representativity. In order to investigate the processability of the powder feedstock and to ensure comparability with other studies, such as [9], a comprehensive characterization of the powder material was carried out. The chemical composition of the material is shown in Table 1, corresponding to the limits specified in the standard DIN EN 1706 [20].

Table 1: Chemical composition of AlSi10Mg powder feedstock material used in this study compared to corresponding alloy standard [20]

Chemical Composition	Al	Si	Mg	Fe	Mn	Cu	Ni	Zn	Pb	Sn	Ti
DIN EN 1706 [20] [Wt.-%]	Bal.	9-11	0.2-0.45	<0.55	<0.45	<0.05	<0.05	<0.1	<0.05	<0.05	<0.15
Concentration [Wt.-%]	Bal.	9.7	0.35	0.1	<0.01	<0.01	<0.01	<0.01	<0.01	<0.01	<0.01

Scanning electron microscope (SEM) images were acquired using a Gemini II (Carl Zeiss AG) for particle morphology analysis and are depicted in Fig. 1. Particles show distinct irregularities and satellite attachments, which can better be detected at a 250x magnification (cf. Fig. 1b). The shape is predominantly non-spherical and has a noticeable proportion of elongated particles. Furthermore, no agglomerates were found.

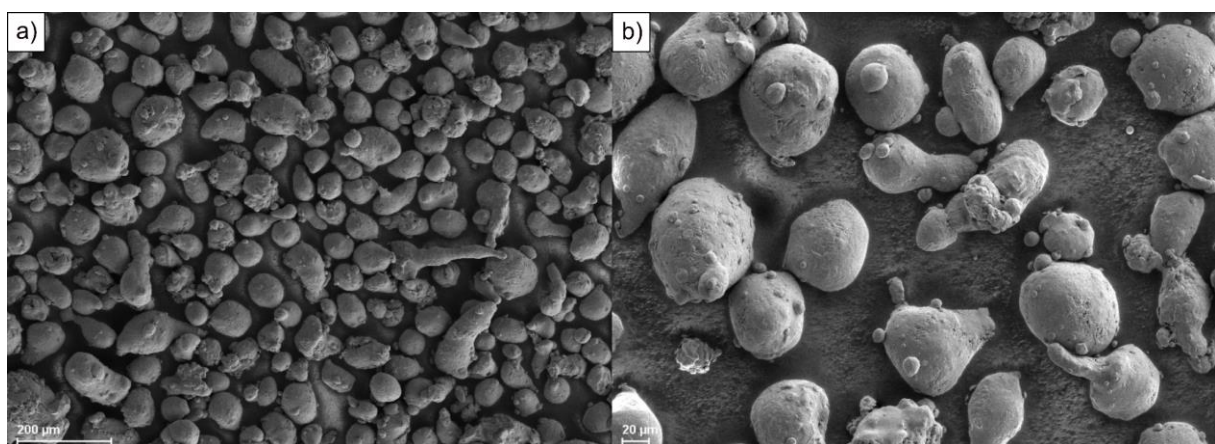


Figure 1: SEM image of powder feedstock material used in this study at 100x magnification a) and 250x magnification b) acquired using a Gemini II (Carl Zeiss AG).

Particle size distribution (measurement of the equivalent projection area) and length-to-width ratio were determined with the dynamic image analysis using the Camsizer X2 with X-Jet module (Microtrac Retsch GmbH) and are shown in Fig. 2. Therefore, the sample was

dispersed at a pressure of 200 kPa. The monomodal, gaussian-like distribution shows a particle range typical for PBF-EB/M-powder with most particles in a size range of 45 μm up to 150 μm (cf. Fig. 2a). The consideration of the width-to-length ratio is consistent with the results of the SEM analysis and confirms the non-spherical shape of the feedstock material. The balance is below 0.9 for all measured particles and forms a maximum between 0.78 and 0.82, which indicates e. g. elongated particles.

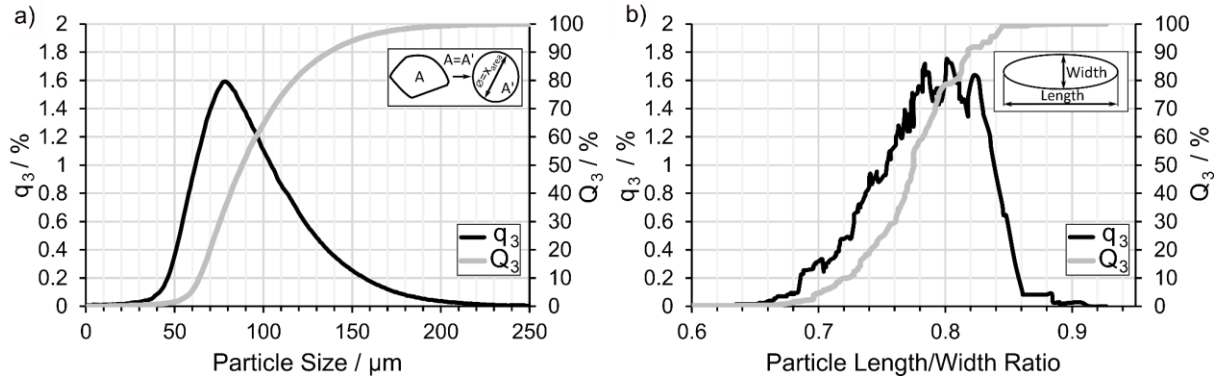


Figure 2: Particle Size distribution a) and particle length to width ratio b) of powder feedstock used in this study measured with Microtrac Retsch GmbH Camsizer (X-Jet method, 200 kPa).

Powder deposition in PBF processes is dynamic and subjects to various influences, such as the coating medium or the powder properties [21]. Further measurements of the flowability and density behavior of the AlSi10Mg powder are presented below. Fig. 3a illustrates the results of the dynamic angle of repose (AR) as well as the cohesive index (CI), which was determined with the GranuDrum (GranuTools). The drum contained a sample of 50 ml powder and was operated at velocities of 2, 4, 6, 8, and 10 rpm. In the first measurement part, the rotating drum increased the rotation speed stepwise from 2 to 10 rpm. Afterwards, the measurement sequence runs reverse in the second part and decreased stepwise from 10 to 2 rpm. This procedure was carried out three times, and the powder position was analyzed using image-based edge detection of images taken at a frame rate of 20 frames per rotation. In addition, the first avalanche angle was determined, at which the drum rotates at a speed of 0.5 rpm until the powder pile collapses. The angle of the measured powder is 37.2°, indicating airflow properties [22]. CI was measured according to the horizontal for each picture and describes the deviation for the AR. The value for CI is near 0 for a non-cohesive powder, which equals a continuous powder flow [23]. The results show a trend with an increasing drum rotation rate, indicating a more irregular powder flow at higher drum rotating speeds. This must be considered when selecting the recoater speed for the powder spreading process in PBF processes.

The tap density of the powder material was measured with a quasi-static method using the GranuPack (GranuTools) based on 1500 taps, as shown in Fig. 3b. A metallic tube was filled with a powder sample of 35 ml. A hollow cylinder provides a flat powder bed during the compaction process. The tube experiences a free fall of 3 mm in height, and a distance sensor measures the position of the hollow cylinder to calculate the density evolution. At the beginning of the measurement, a steep increase in powder density was observed, which gradually approaches a plateau as the number of taps increased. After 1500 taps, a powder density of 1.61 $\text{g}\cdot\text{cm}^{-3}$ was measured. The Hausner ratio, which describes the reduction in volume caused by shaking or tamping, is 1.21 for the measured powder and, therefore exceeds the value of 1, indicating a fair flow character [24]. This is consistent

with the measured values for the angle of repose. The measurement graph confirms that the powder is compacted by the vibration, which can lead to a change in the flow properties.

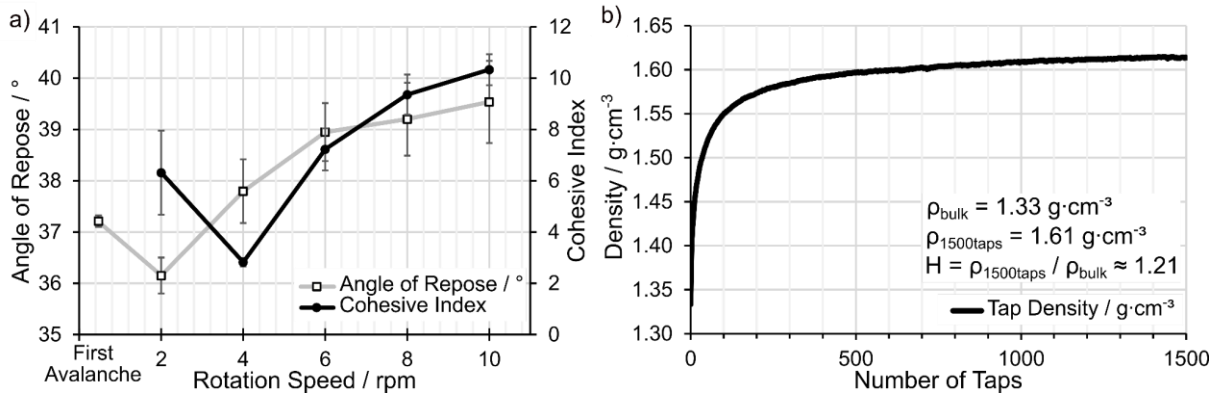


Figure 3: Angle of repose and cohesive index measured with GranuTools GranuDrum a) and tap density measured with GranuTools GranuPack b) of powder feedstock used in this study.

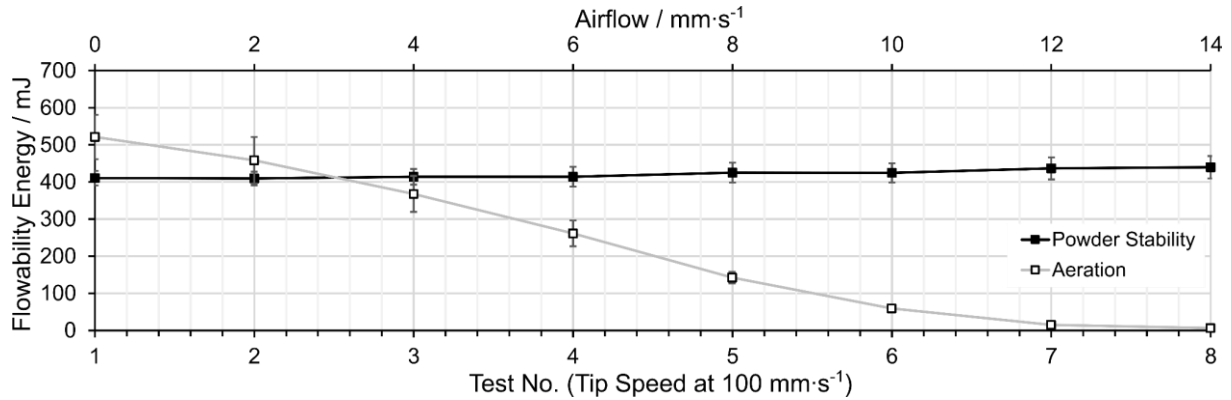


Figure 4: Powder stability- and Aeration Test of the feedstock measured with Freeman Technology Powder Rheometer FT4

The FT4 powder rheometer (Freeman Technology Ltd.) was used for an extended determination of the powder properties using four different measurement methods. Additional powder properties from the FT4 powder rheometer and Hall Flow funnel flowability values are shown in Table 2. Depending on the measurement method, all FT4 procedures were performed with a 25 mm powder cell and a rotating blade or piston. Fig. 4 shows the results of the stability and aeration tests. The stability test includes eight cycles in which the impeller moves into the powder cell in a rotating movement with a tip speed of 100 mm·s⁻¹. The energy the blade must apply to stir through the powder was measured. A conditioning cycle was performed between the test cycles to establish a reproducible state. The results show that the graph is constant, with an average Basic Flowability Energy (BFE) of 436.5 mJ. The Stability Index (SI) represents the ratio between cycles seven and one and describes how the powder is affected when it is made to flow. Therefore, a SI of 1.06 represents a robust and stable powder. The aeration test was performed at different airflow velocities from 0 to 14 mm·s⁻¹. A constant decrease in flowability energy was observed with increasing airflow, from which it can be concluded that there is a relationship between the cohesion of the powder and the air supplied. The aeration ratio was determined from the ratio of the flowability energy at an airflow of

10 mm·s⁻¹ and 0 mm·s⁻¹ and is 9.05. This value indicates an average sensitivity to aeration [25].

Fig. 5 shows the results of the tests performed to determine the compressibility, permeability, and variable flow rate (VFR) of powder feedstock material. VFR describes the flow behavior of the examined powder based on the different tip speeds of the blade. Four cycles were carried out at rates of 100, 70, 40, and 10 mm·s⁻¹. In between, condition cycles were performed. Higher flowability energy is required to move the blade through the powder sample at low tip speeds, as depicted in Fig. 5b. The correlation is since the tested powder exhibits greater cohesive forces at low tip speeds and describes an average flow sensitivity [26]. After three conditioning cycles, a piston was used instead of the blade to measure compressibility and permeability. The measurement is carried out by applying the piston to the powder with increasing normal stress from 1 to 15 kPa. For each pressure applied, the compression is given as a percentage. A maximum compressibility of 3.25 % can be determined for the feedstock powder. Regarding the permeability test, the vessel was connected to a constant airflow of 2 mm·s⁻¹ while increasing stress is applied. The graph shows a constant pressure drop (PD) of approx. 0.8 mbar, describing that compression has little to no effect and results in a high permeability of the powder. Summarizing, the feedstock characterization indicates that the powder feedstock material can be processed regardless of contained irregularly shaped and elongated particles.

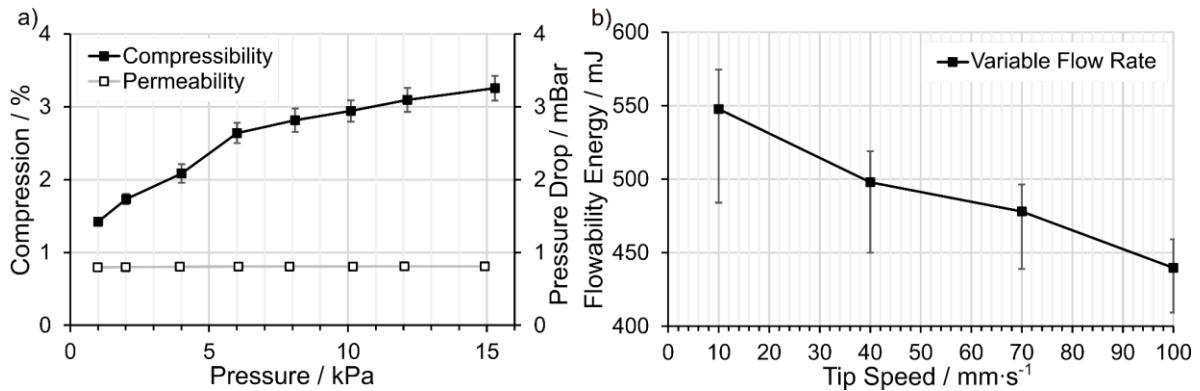


Figure 5: Compressibility and Permeability Test a) and Variable Flow Rate Test b) of the feedstock material measured with Freeman Technology Powder Rheometer FT4.

Table 2: Overview of powder properties of AlSi10Mg powder feedstock material used in this study

Powder Properties	Values
Conditioned Bulk Density / g·ml ⁻¹	1.35
Basic Flowability Energy / mJ	436.54
Stability Index	1.06
Flow Rate Index	1.24
Specific Energy / mJ·g ⁻¹	4.39
Aeration Ratio / mJ	9.05
Compressibility at 15.0 kPa / %	3.25
Pressure Drop at 15.0 kPa / mBar	0.81
Flow Rate / s·(50g) ⁻¹ DIN EN ISO 4490 [27]	81.13
Bulk Density / g·cm ⁻³ DIN EN ISO 3923 [28]	1.28

PBF-EB/M system Freemelt ONE (Freemelt AB) was used to produce specimens ($10 \times 10 \times 10 \text{ mm}^3$) with AlSi10Mg powder feedstock described above. A laser-heated lanthanum hexaboride (LaB₆) cathode and an accelerating voltage of 60 kV were used to generate the electron beam. Build temperature was regulated using an average heat current model as described in Sames et al. [29] and was determined to be 400 °C, which is lower than the sintering temperature of powder feedstock of 435 °C. The sintering temperature was determined experimentally by furnace sintering tests with powder-filled conical weld flanges according to DIN 11865 [30] with a diameter of 40/28 mm and a height of 23 mm in a Nabertherm furnace LH120/12 (Nabertherm GmbH) under Ar shielding gas. The equal packing density for determination of sintering temperature was ensured using a calibrated funnel apparatus (DIN EN ISO 3923-1 [28]). Preheating was performed using prequalified sintering parameters utilizing a defocused electron beam and a linear increase in beam current from 1 mA to the exposure current with a nominal current increase of $1 \text{ mA}\cdot\text{s}^{-1}$, a hatch distance of 1 mm, a nominal beam diameter of 2.5 mm, and a line order of 10, as described in [31]. The samples are exposed with an exposure current of 3.33 mA (200 W) and 8.33 mA (500 W) and a focused electron beam with a nominal beam diameter of 250 μm full width half maximum, which is the minimum focus diameter. Exposure strategy was an incremental spot melting strategy as described in [13] with a spot distance of 100 μm for samples with a beam power of 200 W and 200 μm for samples with a beam power of 500 W and an increment of five for cubic samples, which was varied for the manufacturing of tensile specimens to keep the return time constant for different cross-section sizes. The different spot distance is resulting from the different sizes of the melt pools during exposure and results in adequate overlapping of the melt pools in the cross section. The chemical composition of manufactured samples was measured using the energy-dispersive X-ray fluorescence Olympus VCR equipment with a 4 W X-ray source utilizing a rhodium anode and a silicon drift detector. The relative density of the manufactured samples was analyzed by metallographic cross-section preparation with Opal 410 (QATM) and Saphir 250 A1-ECO (QATM), and by binarization of optical microscope images taken with the VHX-6000 (Keyence) at 200x magnification. The hardness testing was performed using ZHV30 (Zwick-Roell) Vickers hardness testing equipment using 1kgf. The microstructure of the prepared samples was analyzed after cross-section preparation using 10%NaOH etchant. The tensile test was performed using Shimadzu AGX-V 100kN with a test speed of $5 \text{ MPa}\cdot\text{s}^{-1}$ [32].

Results and Discussion

Samples manufactured at a beam power of 200 W consistently show a lack of fusion defects for VED in the range of $16 \text{ J}\cdot\text{mm}^{-3}$ to $42 \text{ J}\cdot\text{mm}^{-3}$, indicating that the applied heat is rapidly conducted away from the site of heat input by the material. Relative density for the mentioned samples is in the range of 78 % to 87 %, also showing high standard deviations. In contrast, specimens manufactured with a beam power of 500 W show an increasing relative density between $12 \text{ J}\cdot\text{mm}^{-3}$ and $20 \text{ J}\cdot\text{mm}^{-3}$ and accepted relative densities of more than 99.5 % for tested VED from $18 \text{ J}\cdot\text{mm}^{-3}$ up to $38 \text{ J}\cdot\text{mm}^{-3}$ with comparatively small standard deviations (see Fig. 6a). However, the samples manufactured with VED higher than $28 \text{ J}\cdot\text{mm}^{-3}$ show swelling on their top surfaces. Hot cracks, which are often observed due to poor melt pool viscosity for aluminum alloys produced by laser powder bed fusion [3, 33–35], are not observed in the manufactured samples. The Vickers hardness of the

manufactured samples is in the range of 14 HV1 to 36 HV1 for an exposure current of 200 W and 40 HV1 to 52 HV1 for exposure currents of 500 W, with standard deviations showing the expected correlation with the sample's relative density. The measured values are significantly lower than the values of 145 HV0.01 [36], 127 HV0.05 [37] and 113-118 HV5 [38] reported for PBF-LB/M samples. This is possibly because material evaporation of magnesium, reported by [9], reduces precipitation hardening, and cooling rates are significantly lower in PBF-EB/M, resulting in a coarser grain structure and Si distribution.

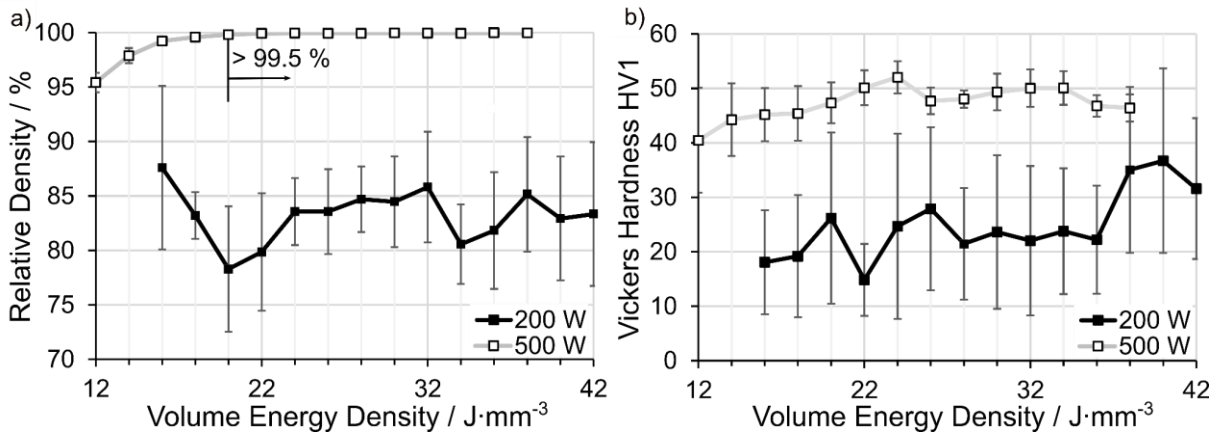


Figure 6: Relative density a) and Vickers Hardness HV1 b) of samples manufactured with 200 W and 500 W exposure current for different volume energy densities. Standard deviation of relative density of samples in a) is not displayed if it is smaller than 0.2 %

Measured Al and Si concentrations for manufactured samples are shown in Fig 7. The samples manufactured with a lower exposure current of 200 W show higher Al evaporation and, thus, higher Si concentration compared to a higher exposure power of 500 W with the same energy input. This could be due to the shorter time of exposure area maintained at elevated temperatures achieved by the energy being delivered within a shorter duration by the beam for samples manufactured with higher beam power. The minimum measured Si concentration of 10.6 % at VED of 32 J·mm⁻³ is close to the initial powder feedstock chemical composition of 9.7 % Si. This indicates that compared to the results of Si concentration of 13.5 % for 200 W and 14.2 % for 300 W reported by the authors [8] for similar energy input and vector-based processing of AlSi10Mg via PBF-EB/M, the applied spot melting strategy with short dwell times is suitable to process materials with volatile elements.

A comparison of the achieved microstructure and tensile properties of spot- and vector-based exposure strategies is described below. Promising parameters for vector-based exposure of test series are reported by the authors [8], utilizing 200 W with a VED of 40 J·mm⁻³, 300 W with a VED of 20 J·mm⁻³, and samples with a spot-based exposure strategy applying a VED of 28 J·mm⁻³ at an exposure beam power of 500 W. Those parameters are used to manufacture tensile specimens. Fig. 8 shows the achieved microstructures revealed by etching with 10%NaOH. The etched microstructures show the dendritic solidification behavior of near-eutectic AlSi10Mg alloy. The microstructure of the samples manufactured with a beam power of 300 W shows a finer distribution of the Si precipitates and lower dendritic arm spacing than those manufactured with a beam power of 200 W, thus indicating higher cooling rates. However, both microstructures achieved by

vector-based exposure (Fig. 8a, b) are showing periodic microstructural changes, possibly due to the layer-upon-layer manufacturing, rotation of vector scanning direction, and thermal heat-affected zones of subsequently manufactured layers. In contrast, the microstructure achieved by a spot-based exposure pattern does not show significant periodic changes or irregularities (Fig. 8c).

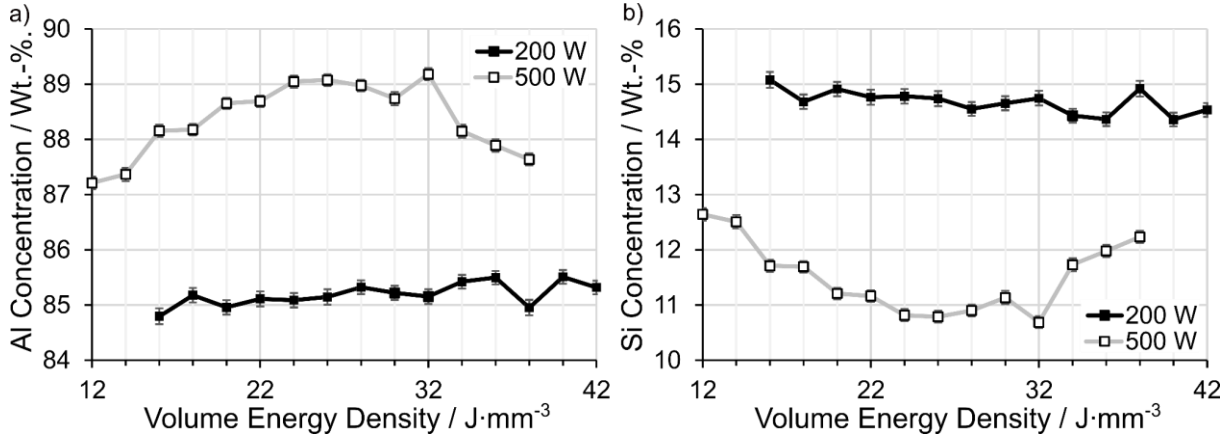


Figure 7: Aluminum a) and silicon b) concentration of samples manufactured with 200 W and 500 W exposure current for different volume energy densities measured using XRF Olympus Vanta C-Series.

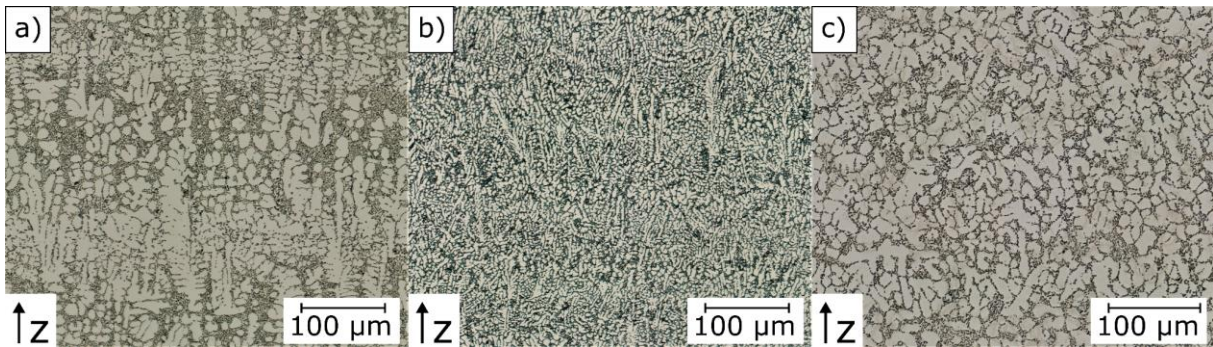


Figure 8: Microstructure of AlSi10Mg samples manufactured with layer height of 100 μm and different exposure strategies, exposure current I , scan speed v and hatch distance h or dwell time d and point distance p : a) vector-based, $I=3.33$ mA, $v=500$ mm·s⁻¹, $h=100$ μm; b) vector-based $I=5$ mA, $v=1500$ mm·s⁻¹ $h=100$ μm; c) spot-based, $I=8.33$ mA, $d=224$ μs, $p=200$ μm

Tensile specimens were manufactured in three orientations. The load direction in the tensile test is perpendicular (90°), at an angle of 45°, and parallel (0°) to the build direction with the parameter sets shown in Fig. 8. The tensile samples were also measured for Si concentration using the XRF measurement method. The samples show Si concentrations of 10.9 Wt.-% (0° and 90°) and 12.7 Wt.-% (45°) for 200 W, 11.9 Wt.-% (90°), 11.3 Wt.-% (0°) and 12.8 Wt.-% (45°) for 300 W samples and 10.1 Wt.-% (90°), 10.6 Wt.-% (0°) and 12.4 Wt.-% (45°) for 500 W samples. Significant higher Si concentrations measured for the 45° samples at the different parameters and exposure strategies indicate higher elemental evaporation of Al, which is assumed to result from increased melt pool temperatures caused by the reduced heat dissipation capability in the overhang region as no support structures are used during manufacturing. The results of the tensile tests are shown in Fig. 9. Specimens manufactured with a point-based exposure

strategy and 500 W show a mean tensile strength of 146 MPa and mean elongation at break values of 27.5 % perpendicular to the build direction. In contrast, specimens manufactured with a vector-based exposure strategy show a mean tensile strength of 66 MPa with mean elongation at a break values of 1.5 % perpendicular to the build direction at 200W and a mean tensile strength of 145 MPa with mean elongation at a break values of 24.5 % perpendicular to the build direction at 300 W. Reduced tensile strength and elongation at break values for samples manufactured with 200 W is attributed to porosity due to the low beam power and the large exposure area of the melted cross-section. At an angle of 45°, tensile specimens manufactured with a point-based exposure strategy show the lowest elongation at break values (7 %) and a mean tensile strength of 113 MPa. In contrast, samples manufactured with 200 W and 300 W show improved mechanical properties with a mean tensile strength of 146 MPa with mean elongation at break values of 22 % for 200 W and a mean tensile strength of 152 MPa with mean elongation at break values of 22 % for 300 W. Parallel to the build direction, specimens manufactured with a vector-based exposure strategy also achieve higher tensile strengths and elongations at break with a mean tensile strength of 141 MPa with mean elongation at break values of 26.5 % at 200 W and a mean tensile strength of 142 MPa with mean elongation at break values of 27 % at 300 W compared to a mean tensile strength of 135 MPa with mean elongation at break values of 16 % for spot-based exposure.

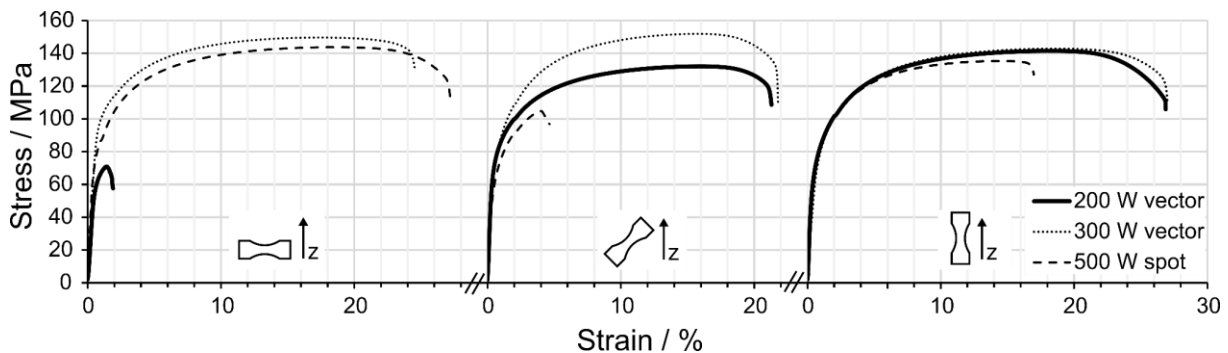


Figure 9: Exemplary representation of tensile test properties in load directions of 90°, 45° and 0° to the build direction of AISi10Mg samples manufactured with a layer height of 100 μm and different exposure strategies, exposure current I , scan speed v , and hatch distance h or dwell time d and point distance p . "200 W vector": vector-based, $I=3.33\text{ mA}$, $v=500\text{ mm}\cdot\text{s}^{-1}$, $h=100\text{ }\mu\text{m}$; 300 W vector: vector-based $I=5\text{ mA}$, $v=1500\text{ mm}\cdot\text{s}^{-1}$ $h=100\text{ }\mu\text{m}$; 500 W spot: spot-based, $I=8.33\text{ mA}$, $d=224\text{ }\mu\text{s}$, $p=200\text{ }\mu\text{m}$. Z indicates the build direction.

The measured properties correlate with a reduced yield strength for AISi10Mg processed at higher temperatures for PBF-LB/M processes with a yield strength of 286 MPa at 35 °C build platform temperature compared to a yield strength of 203 MPa for a build platform temperature of 200 °C reported by Santos Macías et al. [33]. Elongation at break is, however, reported to remain constant at 9.7 % for 35 °C and 9.6 % for 200 °C platform temperature, respectively. This is consistent with a yield strength of 230 MPa to 275 MPa for AISi10Mg samples as reported in [33], and achievable tensile strengths of 282 MPa to 460 MPa and elongation at break values ranging from 1.1 % to 8.8 % for various PBF-LB/M-machines and powders [35].

Fracture surfaces are depicted in Figure 10. The samples manufactured using the vector-based strategy at 200 W show lack of fusion defects with visible sintered powder particles and distributed small damage sites for tensile samples with bigger cross-section sizes, i.e.,

at 90° and 45° to the build direction. This is consistent with reduced elongation at break values measured for the mentioned samples (cf. Fig. 9). In comparison, significantly increased deformed fracture surface areas are visible for specimens with a higher elongation at break. The previously observed reduced elongation at break for the spot-based specimens at an angle of 45° and 0° to the build direction can be reconstructed by analysis of fracture behavior. The interlayer bonding is assumed to have a lower strength than the layers themselves, resulting in a staggered/terraced fracture surface at an angle of 45° and a flat fracture surface at 0° to the build direction. This indicates that the spot-based strategy achieves a weaker interlayer bonding than the vector-based strategy for the utilized process parameters.

Summarized, tensile test properties of samples manufactured via PBF-EB/M exhibit a lower tensile strength than values reported for PBF-LB/M, possibly due to the high build temperature, lower cooling rates, and element evaporation. The achieved elongation at break at PBF-EB/M is superior to values reported for PBF-LB/M.

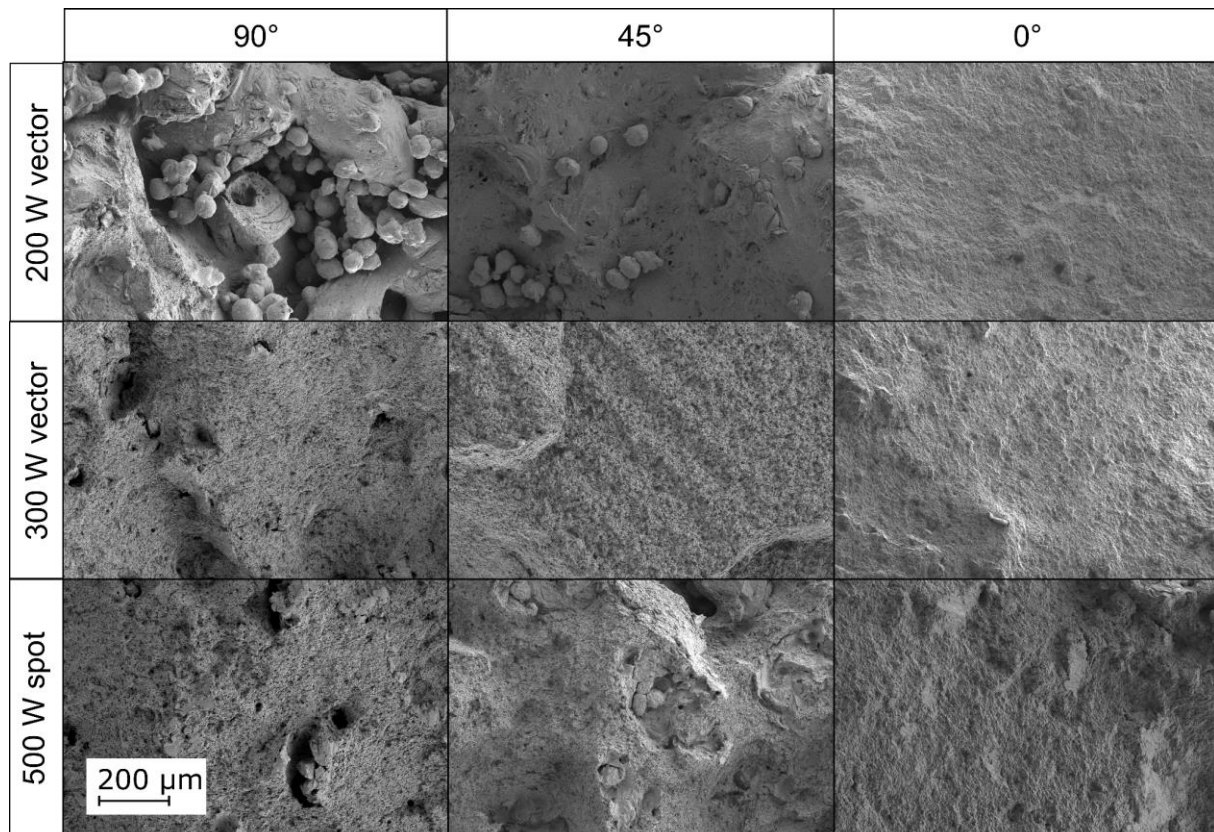


Figure 10: Exemplary representation of fracture surfaces in load directions of 90°, 45° and 0° to the build direction of AlSi10Mg samples manufactured with a layer height of 100 μm and different exposure strategies, exposure current I, scan speed v, and hatch distance h or dwell time d and point distance p. "200 W vector": vector-based, I=3.33 mA, v=500 mm·s⁻¹, h=100 μm; 300 W vector: vector-based I=5 mA, v=1500 mm·s⁻¹ h=100 μm; 500 W spot: spot-based, I=8.33 mA, d=224 μs, p=200 μm.

Conclusion

This study evaluated the processability of AlSi10Mg in PBF-EB/M using an incremental spot-based exposure algorithm based on an extensive characterization of powder feedstock. Sample properties and microstructure are reported and compared to achievable properties using a vector-based exposure strategy in PBF-EB/M and PBF-LB/M. While spot-based exposure with an electron beam power of 200 W leads to significant lack of fusion defects, relative densities of 99.9 % could be achieved using 500 W exposure beam power. Here, AlSi10Mg components obtain a hardness of up to 52 HV1 and tensile strengths of up to 152 MPa with superior elongation at break values of up to 27 % compared to PBF-LB/M. Spot-based exposure patterns have also been shown to be suitable for manufacturing alloys with volatile elements by reducing the element loss compared to vector-based exposure strategies. Further research is needed to investigate, on the one hand, the evaporation of elements not detectable in this study, such as magnesium. On the other hand, further experiments or simulations are needed to evaluate the possibilities of further reducing volatile element evaporation.

This could be done, for example, through improved process control and exposure algorithms that focus on a shorter time to maintain the exposure area at high temperatures while investigating higher energy inputs to ensure bonding between the layers and improve tensile properties for load directions that are not perpendicular to the build direction.

Contact details

Robert Ortmann (corresponding author)
Universitätsstraße 150, 44801 Bochum
E-Mail: robert.ortmann@rub.de
WEB: <https://www.ham.ruhr-uni-bochum.de/>

References

1. DIN EN ISO/ASTM 52900:2022-03, Additive Fertigung- Grundlagen-Terminologie (ISO/ASTM 52900:2021); Deutsche Fassung EN ISO/ASTM 52900:2021 01.040.25, 25.030(DIN EN ISO/ASTM 52900:2022-03)
2. Aversa A, Marchese G, Saboori A et al. (2019) New Aluminum Alloys Specifically Designed for Laser Powder Bed Fusion: A Review. *Materials (Basel)* 12. <https://doi.org/10.3390/ma12071007>
3. Aboulkhair NT, Everitt NM, Maskery I et al. (2017) Selective laser melting of aluminum alloys. *MRS Bull* 42:311–319. <https://doi.org/10.1557/mrs.2017.63>
4. Sing SL, An J, Yeong WY et al. (2016) Laser and electron-beam powder-bed additive manufacturing of metallic implants: A review on processes, materials and designs. *J Orthop Res* 34:369–385. <https://doi.org/10.1002/jor.23075>
5. Bieske J, Franke M, Schloffer M et al. (2020) Microstructure and properties of TiAl processed via an electron beam powder bed fusion capsule technology. *Intermetallics* 126:106929. <https://doi.org/10.1016/j.intermet.2020.106929>

6. Juechter V, Scharowsky T, Singer RF et al. (2014) Processing window and evaporation phenomena for Ti-6Al-4V produced by selective electron beam melting. *Acta Materialia* 76:252–258.
<https://doi.org/10.1016/j.actamat.2014.05.037>
7. Klassen A, Forster VE, Juechter V et al. (2017) Numerical simulation of multi-component evaporation during selective electron beam melting of TiAl. *Journal of Materials Processing Technology* 247:280–288.
<https://doi.org/10.1016/j.jmatprotec.2017.04.016>
8. Kretzer N, Ortmann R, Grimm T et al. Einfluss von Prozessparametern auf die chemische Zusammensetzung von AlSi10Mg-Bauteilen beim pulverbettbasierten Elektronen-Strahlschmelzen. In: *Tagung Werkstoffprüfung 2022*, vol 40, pp 111–116
9. Bian H, Aoyagi K, Zhao Y et al. (2020) Microstructure refinement for superior ductility of Al-Si alloy by electron beam melting. *Additive Manufacturing* 32:100982. <https://doi.org/10.1016/j.addma.2019.100982>
10. Mollamahmutoglu M, Yilmaz O, Unal R et al. (2022) The effect of evaporation and recoil pressure on energy loss and melt pool profile in selective electron beam melting. *Int J Adv Manuf Technol* 120:4041–4050.
<https://doi.org/10.1007/s00170-022-09017-2>
11. Gu D, Shen Y (2009) Balling phenomena in direct laser sintering of stainless steel powder: Metallurgical mechanisms and control methods. *Materials & Design* 30:2903–2910. <https://doi.org/10.1016/j.matdes.2009.01.013>
12. Lee YS, Kirka MM, Raghavan N, Dehoff RR (2017) Simulation of Spot Melting Scan Strategy to Predict Columnar to Equiaxed Transition in Metal Additive Manufacturing. In: *Solid Freeform Fabrication 2017*, pp 1005–1017
13. Raghavan N, Dehoff R, Pannala S et al. (2016) Numerical modeling of heat-transfer and the influence of process parameters on tailoring the grain morphology of IN718 in electron beam additive manufacturing. *Acta Materialia* 112:303–314. <https://doi.org/10.1016/j.actamat.2016.03.063>
14. Raghavan N, Simunovic S, Dehoff R et al. (2017) Localized melt-scan strategy for site specific control of grain size and primary dendrite arm spacing in electron beam additive manufacturing. *Acta Materialia* 140:375–387. <https://doi.org/10.1016/j.actamat.2017.08.038>
15. Dehoff RR, Kirka MM, Sames WJ et al. (2015) Site specific control of crystallographic grain orientation through electron beam additive manufacturing. *Materials Science and Technology* 31:931–938.
<https://doi.org/10.1179/1743284714Y.0000000734>
16. Halsey W, Ferguson J, Plotkowski A et al. (2020) Geometry-independent microstructure optimization for electron beam powder bed fusion additive manufacturing. *Additive Manufacturing* 35:101354.
<https://doi.org/10.1016/j.addma.2020.101354>

17. Plotkowski A, Ferguson J, Stump B et al. (2021) A stochastic scan strategy for grain structure control in complex geometries using electron beam powder bed fusion. *Additive Manufacturing* 46:102092.
<https://doi.org/10.1016/j.addma.2021.102092>
18. Shao M, Vijayan S, Nandwana P et al. (2020) The effect of beam scan strategies on microstructural variations in Ti-6Al-4V fabricated by electron beam powder bed fusion. *Materials & Design* 196:109165.
<https://doi.org/10.1016/j.matdes.2020.109165>
19. DIN EN ISO 3954:2007-11, Pulver für die Pulvermetallurgie - Probenahme (ISO 3954:2007); Deutsche Fassung EN ISO 3954:2007
20. DIN EN 1706:2021-10, Aluminium und Aluminiumlegierungen -Gussstücke- Chemische Zusammensetzung und mechanische Eigenschaften; Deutsche Fassung EN 1706:2020+A1:2021
21. Spierings AB, Voegtlin M, Bauer T et al. (2016) Powder flowability characterisation methodology for powder-bed-based metal additive manufacturing. *Prog Addit Manuf* 1:9–20.
<https://doi.org/10.1007/s40964-015-0001-4>
22. Basavaraj B, Saritha N, Bharath S et al. (2013) Vigna Mungo Mucilage - A Natural Polymer in the Design of Matrix Based SR Tablet of Aceclofenac. *International Journal of Pharmaceutical Sciences Review and Research*:125–130
23. Lumay G, Boschini F, Traina K et al. (2012) Measuring the flowing properties of powders and grains. *Powder Technology* 224:19–27.
<https://doi.org/10.1016/j.powtec.2012.02.015>
24. Fitzpatrick J (2013) *Handbook of food powders: Processes and properties*. Woodhead publishing series in food science, technology and nutrition, vol 255. Woodhead Publ, Oxford .
25. Freeman R (2007) Measuring the flow properties of consolidated, conditioned and aerated powders — A comparative study using a powder rheometer and a rotational shear cell. *Powder Technology* 174:25–33.
<https://doi.org/10.1016/j.powtec.2006.10.016>
26. Freeman R (2005) Measuring the flow properties of consolidated, conditioned and aerated powders – a comparative study using a powder rheometer and a rotational shear cell. In: *Particulate Systems Analysis*, Stratford 2005
27. DIN EN ISO 4490:2018-08, Metallpulver - Bestimmung der Durchflussrate mit Hilfe eines kalibrierten Trichters (Hall flowmeter) (ISO 4490:2018); Deutsche Fassung EN ISO 4490:2018
28. DIN EN ISO 3923-1:2018-10, Metallpulver - Ermittlung der Füll-dichte- Teil 1: Trichterverfahren (ISO 3923-1:2018); Deutsche Fassung EN ISO 3923-1:2018

29. Sames WJ (2015) Additive Manufacturing of Inconel718 using Electron Beam Melting: Processing, post-process, & mechanical properties. Dissertation, Texas A&M University
30. DIN 11865:2020-07, Komponenten aus nichtrostendem Stahl für aseptische Anwendungen in der chemischen und pharmazeutischen Industrie - T-Stücke, Bogen und Reduzierstücke
31. Karimi P, Sadeghi E, Ålgårdh J et al. (2021) Tailored grain morphology via a unique melting strategy in electron beam-powder bed fusion. *Materials Science and Engineering: A* 824:141820.
<https://doi.org/10.1016/j.msea.2021.141820>
32. DIN EN ISO 6892-1:2020-06, Metallische Werkstoffe - Zugversuch - Teil 1: Prüfverfahren bei Raumtemperatur (ISO 6892-1:2019); Deutsche Fassung EN ISO 6892-1:2019
33. Santos Macías JG, Douillard T, Zhao L et al. (2020) Influence on microstructure, strength and ductility of build platform temperature during laser powder bed fusion of AlSi10Mg. *Acta Materialia* 201:231–243.
<https://doi.org/10.1016/j.actamat.2020.10.001>
34. Kang N, Coddet P, Chen C et al. (2016) Microstructure and wear behavior of in-situ hypereutectic Al–high Si alloys produced by selective laser melting. *Materials & Design* 99:120–126.
<https://doi.org/10.1016/j.matdes.2016.03.053>
35. Asgari H, Baxter C, Hosseinkhani K et al. (2017) On microstructure and mechanical properties of additively manufactured AlSi10Mg 200C using recycled powder. *Materials Science and Engineering: A* 707:148–158.
<https://doi.org/10.1016/j.msea.2017.09.041>
36. Buchbinder D, Schleifenbaum H, Heidrich S et al. (2011) High Power Selective Laser Melting (HP SLM) of Aluminum Parts. *Physics Procedia* 12:271–278. <https://doi.org/10.1016/j.phpro.2011.03.035>
37. Kempen K, Thijs L, van Humbeeck J et al. (2012) Mechanical Properties of AlSi10Mg Produced by Selective Laser Melting. *Physics Procedia* 39:439–446.
<https://doi.org/10.1016/j.phpro.2012.10.059>
38. Serjouei A, Libura T, Brodecki A et al. (2022) Strength-hardness relationship for AlSi10Mg alloy produced by laser powder bed fusion: An experimental study. *Materials Science and Engineering: A* 861:144345.
<https://doi.org/10.1016/j.msea.2022.144345>